

Radar backscattering from Gerstner's sea surface wave

Iosif M Fuks¹ and Alexander G Voronovich²

¹ Zel Technologies, LLC and NOAA/Environmental Technology Laboratory, 325 Broadway, Boulder, CO 80305, USA

² NOAA/Environmental Technology Laboratory, 325 Broadway, Boulder, CO 80305, USA

Received 5 December 2001, in final form 1 March 2002

Published 4 April 2002

Online at stacks.iop.org/WRM/12/321

Abstract

In the framework of a two-scale scattering model, radar backscattering from the rough sea surface was considered. The sea surface was modelled as a superposition of a nonlinear, large-scale Gerstner's wave and small-scale resonant Bragg scattering ripples. The zero-order diffracted field was found by a geometrical optics approach, with shadowing taken into account, and by an 'exact' solution of the diffraction problem obtained numerically. For vertical and horizontal polarizations, the spatial distribution of specific scattering cross sections along the large-scale wave was obtained. The spatially averaged specific backscattering cross sections, as well as the mean Doppler frequency shifts at both polarizations, obtained by the geometrical optics approach are compared with those obtained by using the 'exact' solution of the large-scale diffraction problem. The roles of shadowing and multiple wave scattering processes are discussed, and qualitative explanations of the difference between these two approaches are given.

1. Introduction

The phenomena of radio wave scattering by a rough sea surface has been attracting the attention of scientists and engineers for many decades, since the 1940s when the first radars were built. In the 1950s and 1960s the theory of long (hundreds of metres) radio wave scattering was developed, which could explain almost all experimental results obtained by that time for this wave band (see, e.g., references in [1, 2]). Based on the first order of the small perturbation method (the small parameter is the ratio of the sea wave height to the radio wavelength) this theory gave a satisfactory explanation of scattered signal power dependence on the sea state and observed frequency Doppler shift (which does not depend on the sea state within the framework of this theory!). For short radio waves (HF wave band) the higher orders of the small perturbation method were invoked to interpret the shape of the Doppler spectrum and its width, which is very sensitive to the sea state. To achieve better agreement with the

experimental results, a more precise description of the sea surface dynamics (including some nonlinear hydrodynamic effects) was necessary [3, 4].

Modelling the scattering of the shorter radio waves (decimetre and centimetre wavelengths) turned out to be more complex. The essential step in the theoretical approach to solving this problem was the introduction of a ‘two-scale’ scattering model; it was first suggested in [5] for scalar waves and then generalized for electromagnetic waves in [6] and [7]. The essence of this model is the assumption that scattering of short radio waves has a resonant nature, i.e. it is caused by small ripples with a wavelength of the order of the radio wave wavelength. The large-scale components of sea roughness only modulate this scattering process owing to the variation of local grazing angle between the incident wave propagation direction and the local sea slope. The principal defect of this theory is the arbitrary splitting of the sea roughness spectrum into ‘small ripples’ and ‘large waves’ parts. Nevertheless, it could explain (at least, qualitatively) many features of scattered radio signals, including scattered power dependence on wind speed, Doppler spectra and frequency shift, and polarization effects [8, 9].

The two-scale model in its simplest form does not take into account the diffraction and multiple scattering effects associated with long waves. Meanwhile, the multiple scattering processes and shadowing (in other words, non-local interaction between the wave field and the surface) may play a significant role for propagation at low grazing angles. One possible approach for taking into account the non-local effects is to separate the propagation process from the scattering one. By *propagation* we mean diffraction of the wave field on its way to and from the scattering area of the rough surface. The scattering process is local and could be described by the small perturbation method, but the wave that illuminates this scattering patch of rough surface differs from the incident wave because it interacts with the long-wave component of the rough surface as it propagates above it. This problem was separated into two parts (propagation and scattering) in [10] to solve the problem of calculating a scattering cross section from a rough surface at small grazing angles. The same idea is used in [11] to explain the polarization anomalies in a backscattering cross section from a rough sea surface by considering incident- and scattered-wave diffraction by the triangular shape of the sea crests (or multiple scattering by concave sea troughs in [12]) before and after backscattering by small ripples on the surface of the large-scale sea waves.

Later, the influence of the large-scale, steep component of sea roughness was considered in the framework of a two-scale model not only as a local slope modulation factor but as a cause of anomalies of zero-order (unperturbed) field strength calculated numerically and resulting from wave diffraction by a steep isolated bump at the sea surface [13, 14]. In this paper, we consider a more realistic model of large-scale sea roughness, namely, the nonlinear surface Gerstner’s waves. In the framework of the two-scale model, the zero-order field is calculated by two approaches: an approximation by geometrical optics (with shadowing taken into account) and an exact (numerical) solution of wave diffraction by Gerstner’s wave profile. In contrast to other studies, which apply a numerical solution to the diffraction problem as a whole (see, e.g., [15] and references to earlier works there) we used a numerical approach only to calculate the zero-order solution for the field diffracted by the large-scale surface structure (the Gerstner’s wave). The backscattering from the small-scale Bragg resonant ripples, which covers this large-scale surface wave, is considered in the framework of the first-order small perturbation theory.

In section 2, we briefly introduce the main equations pertinent to the two-scale scattering model. Section 3 addresses the issue of Gerstner’s wave hydrodynamics and gives a geometrical description. In section 4 we present the computational results for specific scattering cross sections and Doppler frequency spectra, obtained by a geometrical optics approach for the zero-order field as well as by a numerical solution for an incident field diffracted by Gerstner’s wave, are presented. We summarize, compare, and discuss these results in section 5.

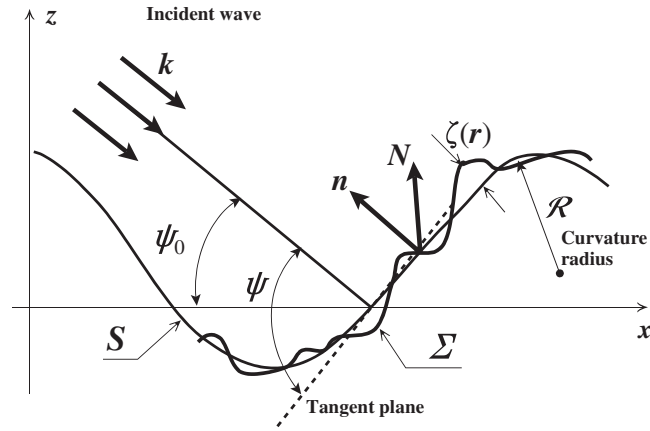


Figure 1. Geometry of scattering.

2. Two-scale model of wave scattering by an impedance rough surface

We consider the scalar monochromatic wave field $U(\mathbf{R})$ (assuming a time dependence of $\exp(-i\omega_0 t)$) that is a solution of the Helmholtz equation

$$(\Delta_{\mathbf{R}} + k^2)U(\mathbf{R}) = 0. \quad (1)$$

Here, \mathbf{R} is a radius vector in three-dimensional space, $k = \omega_0/c_0 = 2\pi/\lambda$ is the wavenumber, λ is the wavelength and c_0 is the velocity of light. Field $U(\mathbf{R})$ is supposed to satisfy the impedance boundary condition on the rough surface Σ (see figure 1):

$$\left. \frac{\partial U}{\partial N} + ik\eta U \right|_{\Sigma} = 0, \quad (2)$$

where $\partial/\partial N$ denotes the normal derivative at the surface Σ , and η is the normal surface impedance. Equations (1) and (2) also describe the electromagnetic wave propagation and scattering in two-dimensional space, when we consider separately the vertically polarized transverse-magnetic (TM) waves, in which the magnetic field vector is perpendicular to the plane of incidence, and the horizontally polarized transverse-electric (TE) waves, in which the electric field vector is perpendicular to the plane of incidence. They are scattered by the rough boundary Σ with a generally complex dielectric permittivity ε , which is assumed to be large ($|\varepsilon| \gg 1$). For these two polarizations, impedance η has the form³:

$$\eta = \begin{cases} 1/\sqrt{\varepsilon} & \text{for vertical polarization (TM wave)} \\ \sqrt{\varepsilon} & \text{for horizontal polarization (TE wave)}. \end{cases} \quad (3)$$

Along with the rough surface Σ , we consider the smooth, undulating surface S (figure 1). We assume that the surface Σ can be represented as small normal deviations $\zeta(\mathbf{r})$ ($\mathbf{r} \in S$) from S , and suppose that the typical radius of curvature \mathcal{R} of S is large compared with the wavelength λ and the condition $k\mathcal{R} \gg 1$ holds. Assuming that the slopes $\gamma(\mathbf{r}) = \nabla_{\mathbf{r}}\zeta(\mathbf{r})$ of roughness $\zeta(\mathbf{r})$ ($\mathbf{r} \in S$) with respect to S are also small ($\gamma^2 \ll 1$), we can expand the boundary condition (2) in powers of $\zeta(\mathbf{r})$ and retain only the first-order terms $\sim O(\zeta)$ (see, e.g., [8]).

³ For small grazing angles, the more precise equations have the form $\eta = 1/\sqrt{\varepsilon + 1}$ for the TM wave, and $\eta = \sqrt{\varepsilon - 1}$ for the TE wave. Since our consideration is not restricted by small grazing angle propagation only, we use (3) for all range of incidence angles.

The solution of the diffraction problem can be represented in the form $U = U_0 + u$, where U_0 is the unperturbed wave field corresponding to the diffraction by the smooth surface S , and u is a correction to the first order of $\zeta(\mathbf{r})$, that is, the scattered field. The zero-order field U_0 satisfies the Helmholtz equation (1) and the uniform boundary condition

$$\left. \frac{\partial U_0}{\partial n_S} + ik\eta U_0 \right|_S = 0, \quad (4)$$

here, n_S is the unit vector normal to the smoothed surface S .

Using Green's theorem and assuming that the condition $k\mathcal{R}|\sqrt{\varepsilon}| \gg 1$ holds, (see [13] and [12] for details) we can represent the scattered field u at the arbitrary point \mathbf{R} as the following surface integral:

$$u(\mathbf{R}) = \iint_S \zeta(\mathbf{r}) \left\{ \begin{array}{l} k^2[1 - \eta^2]G_0(\mathbf{R}, \mathbf{r})U_0(\mathbf{r}) \\ -\nabla_r G_0(\mathbf{R}, \mathbf{r})\nabla_r U_0(\mathbf{r}) \end{array} \right\} d\mathbf{r}. \quad (5)$$

Here, the surface gradient ∇_r is calculated along the local plane tangent to S at point \mathbf{r} , and Green's function $G_0(\mathbf{R}, \mathbf{R}')$ of the boundary problem for S is introduced:

$$(\Delta_{\mathbf{R}} + k^2)G_0(\mathbf{R}, \mathbf{R}') = -\delta(\mathbf{R} - \mathbf{R}'), \quad (6)$$

$$\left. \frac{\partial G_0(\mathbf{R}, \mathbf{r})}{\partial n_S} + ik\eta G_0(\mathbf{R}, \mathbf{r}) \right|_{\mathbf{r} \in S} = 0. \quad (7)$$

Equation (5) represents the general solution of the scattering problem to the first order in ζ .

Hereinafter, we consider scattering of an incident plane wave $U_{inc}(\mathbf{R}) = \exp(i\mathbf{k}\mathbf{R})$, where \mathbf{k} is the wavevector with the projections $k_x = k \cos \psi_0$, $k_y = 0$, $k_z = -k \sin \psi_0$. We use the Cartesian coordinate system in which the $\{x, z\}$ plane is chosen as the plane of incidence, and ψ_0 is the grazing angle (figure 1) relative to the plane $z = 0$. The total unperturbed field $U_0(\mathbf{r})$ on S can be represented in the form

$$U_0(\mathbf{r})|_S = U_{inc}(\mathbf{r}) + U_{ref}(\mathbf{r}) = F(\mathbf{r})e^{i\mathbf{k}\mathbf{r}}, \quad \mathbf{r} \in S, \quad (8)$$

where U_{ref} is the reflected wave and $F(\mathbf{r})$ is assumed to be a slowly varying function on S (in comparison with the phase factor $e^{i\mathbf{k}\mathbf{r}}$: $|\nabla_r F| \ll kF$). From the reciprocity principle, it follows that Green's function $G_0(\mathbf{R}, \mathbf{r})$ is equal to $G_0^*(\mathbf{r}, \mathbf{R})$, which in turn can be represented as a Fourier expansion into plane waves. Each of these waves generates field $U_0(\mathbf{r})$ on the surface S , given by (8). The stationary phase method, applied to the corresponding Fourier integral, leads to the following expression for Green's function $G_0(\mathbf{R}, \mathbf{r})$ in the far zone:

$$G_0(\mathbf{R}, \mathbf{r}) = \frac{e^{i\mathbf{k}\mathbf{R}}}{4\pi R} F(\mathbf{r})e^{i\mathbf{k}\mathbf{r}}. \quad (9)$$

Substituting (8) and (9) into (5), we obtain [12]

$$u(\mathbf{R}) = \frac{e^{i\mathbf{k}\mathbf{R}}}{4\pi R} \iint_S \zeta(\mathbf{r}) [k^2(1 - \eta^2) + k_{\perp}^2] e^{2i\mathbf{k}\mathbf{r}} F^2(\mathbf{r}) d\mathbf{r}, \quad (10)$$

where $k_{\perp} = k \cos \psi$ is the projection of the wavevector \mathbf{k} on the plane tangent to S at the point \mathbf{r} , and ψ is a local grazing angle (see figure 1). Below, we assume that the surface roughness $\zeta(\mathbf{r})$ is a spatially homogeneous random function of the spatial coordinate \mathbf{r} , and we denote statistical averaging in chevron brackets $\langle \dots \rangle$. Our goal is to estimate the average backscatter power that is proportional to $\langle |u(\mathbf{R})|^2 \rangle$. It follows from (10) that calculation of $\langle |u(\mathbf{R})|^2 \rangle$ leads to the appearance in the integrand of the autocorrelation function $W(\boldsymbol{\rho}) = \langle \zeta(\mathbf{r})\zeta(\mathbf{r} + \boldsymbol{\rho}) \rangle$ in which the spatial scale of variation l (correlation radius) is assumed to be small in comparison

with the spatial variation scale L of $F(\mathbf{r})$. On the basis of these assumptions, we obtain from (10)

$$\langle |u(\mathbf{R})|^2 \rangle = \frac{1}{4R^2} \iint_S \mathcal{S}_\zeta(2\mathbf{k}_\perp) |k^2(1 - \eta^2) + k_\perp^2|^2 |F(\mathbf{r})|^4 d\mathbf{r}. \quad (11)$$

Here, the spatial power spectrum $\mathcal{S}_\zeta(\mathbf{q})$ of stochastic roughness $\zeta(\mathbf{r})$ is introduced:

$$\mathcal{S}_\zeta(\mathbf{q}) = \frac{1}{(2\pi)^2} \iint_{-\infty}^{\infty} W(\boldsymbol{\rho}) e^{i\mathbf{q}\boldsymbol{\rho}} d\boldsymbol{\rho}. \quad (12)$$

According to the definition, we obtain from (11) the following equation for the backscattering cross section σ_{tot} from the whole illuminated surface S (the zero-order field U_0 is not included):

$$\sigma_{tot} = 4\pi \frac{\langle |u(\mathbf{R})|^2 \rangle}{R^2 |U_{inc}|^2} = \iint_S \sigma_0(\mathbf{r}) d\mathbf{r}, \quad (13)$$

where the specific scattering cross section $\sigma_0(\mathbf{r})$ is introduced:

$$\sigma_0(\mathbf{r}) = 16\pi k^4 \mathcal{S}_\zeta(2k \cos \psi, 0) C(\psi, \mathbf{r}). \quad (14)$$

Following [13], we introduce the scattering coefficient $C(\psi, \mathbf{r})$:

$$C(\psi, \mathbf{r}) = \frac{1}{16} |1 - \eta^2 + \cos^2 \psi|^2 |F(\mathbf{r})|^4. \quad (15)$$

We emphasize that the scattering coefficient $C(\psi, \mathbf{r})$ depends not only on the local grazing angle ψ but also on coordinate \mathbf{r} because of the non-local dependence between the field $U_0(\mathbf{r})$ and S .

If we assume that, at each point \mathbf{r} of smoothed surface S , Green's function $G_0(\mathbf{R}, \mathbf{r})$ and the unperturbed field $U_0(\mathbf{r})$ are the same as for the plane tangent to S (the so-called *tangent plane* or *Kirchhoff approximation*), we obtain the well known two-scale scattering model that was first suggested for scalar wave scattering in [5], and then generalized for electromagnetic wave scattering in [6] and [9]. In the tangent plane approximation, the term $U_{ref}(\mathbf{r})$ in (8) is assumed to coincide with the specular reflected wave from the plane tangent to S with the local reflection coefficient $V(\psi) = (\sin \psi - \eta)/(\sin \psi + \eta)$. In this case we have

$$F \Rightarrow F_0(\psi) = 1 + V(\psi) = \frac{2 \sin \psi}{\sin \psi + \eta}, \quad (16)$$

$$C \Rightarrow C_0(\psi) = |1 - \eta^2 + \cos^2 \psi|^2 \left| \frac{\sin \psi}{\sin \psi + \eta} \right|^4. \quad (17)$$

For a perfectly conducting surface S , the last equation leads to the well known simple expressions for the scattering coefficient (see, e.g., [8]):

$$C_0(\psi) = \begin{cases} (1 + \cos^2 \psi)^2 & \text{for vertical polarization } (\eta = 0) \\ \sin^4 \psi & \text{for horizontal polarization } (\eta = \infty). \end{cases} \quad (18)$$

Equation (14) gives the specific scattering cross section $\sigma_0(\mathbf{r})$ relating to the unit area of surface S . The specific scattering cross section $\bar{\sigma}_0(\mathbf{r})$ relating to the unit area of the surface S projection on the plane $z = 0$ is given by the same equation with the obvious substitution

$$C(\psi, \mathbf{r}) \Rightarrow \tilde{C}(\psi, \mathbf{r}) = C(\psi, \mathbf{r})/n_z(\mathbf{r}) \quad (19)$$

where $n_z(\mathbf{r})$ is the projection of the normal vector \mathbf{n} of surface S on the Oz axis.

3. Gerstner's rotational waves

3.1. Kinematic description

Here we consider the simplest model of nonlinear sea surface waves, which does not require small wave slopes, and is an exact solution of nonlinear hydrodynamic equations for surface gravity waves for fluid of infinite depth. This solution was obtained in 1802 by Gerstner, but it detracts somewhat from the physical interest of the results because the fluid motion in these waves cannot be described by introducing the velocity potential. The generation of these waves under realistic conditions is not clear, since they are rotational. Thus, interest in these waves has been limited. Use Gerstner's simple analytical description of a rotational wave significantly simplifies the study of scattering and enables results to be obtained in analytical form. On the other hand, the geometrical structure of Gerstner's waves is similar to the structure of Stokes's waves in many important respects.

The coordinates (x, z) of a liquid particle in a Gerstner's wave depend on time τ as follows (see, e.g., [16] p 421, and [17] p 158):

$$\begin{aligned} x &= x_0 - ae^{Kz_0} \sin[K(x_0 - c\tau)], \\ z &= z_0 + ae^{Kz_0} \cos[K(x_0 - c\tau)], \end{aligned} \quad (20)$$

where $K = 2\pi/\Lambda$ is the wavenumber of the surface wave, Λ is the wavelength, $c = \sqrt{g/K}$ is the wave propagation velocity, g is the gravity acceleration, a is the wave amplitude, (x_0, z_0) are two parameters identifying a particle. For $z_0 = 0$ (which corresponds to the particles on the water surface) we obtain from (20)

$$\begin{aligned} x &= x_0 - a \sin[K(x_0 - c\tau)], \\ z &= a \cos[K(x_0 - c\tau)]. \end{aligned} \quad (21)$$

The particle velocity v in an immovable coordinate system is

$$\begin{aligned} v_x &= dx/d\tau = v_0 \cos[K(x_0 - c\tau)], \\ v_z &= dz/d\tau = v_0 \sin[K(x_0 - c\tau)], \end{aligned} \quad (22)$$

where $v_0 = aKc = a\omega$; $\omega = \sqrt{gK}$. In the coordinate system moving with the wave profile with velocity c (i.e. with replacement $x - ct \Rightarrow x$) the surface equation takes the parametric form

$$x = t/K - a \sin t, \quad z = a \cos t, \quad (23)$$

where $t = K(x_0 - c\tau)$. This is a trochoid's equation. The equations for the other trochoid parameters are

$$\text{orbital velocity } v_x = v_0 \cos t, \quad v_z = v_0 \sin t, \quad (24)$$

$$\text{surface slope } \gamma = dz/dx = -\frac{b \sin t}{1 - b \cos t}, \quad (25)$$

where the steepness parameter $b = aK$ is introduced. The maximum surface slope γ_m corresponds to the point where $\cos t = b$, and it is given by the equation

$$\gamma_m = \frac{b}{\sqrt{1 - b^2}}. \quad (26)$$

Note that the trochoid's maximum slope in (26) always exceeds that of the sinusoid ($\gamma_m = b$) with the same amplitude a and wavelength Λ . For small values of parameter b , the trochoid equation (23) coincides with that of the sinusoid $z = a \cos Kx$, but when b approaches unity, the surface shape near the tops becomes more and more steep, and the position of the maximum

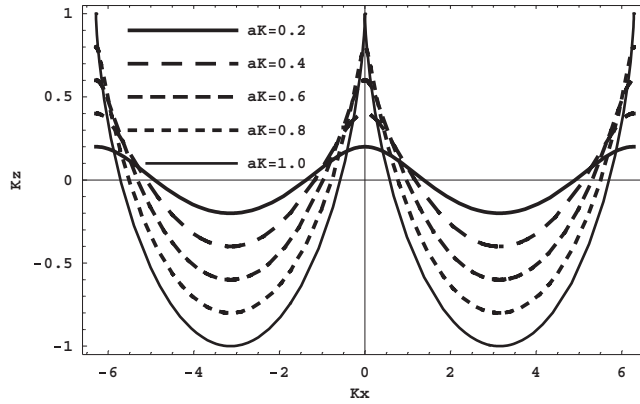


Figure 2. Trochoids with different steepness parameter aK .

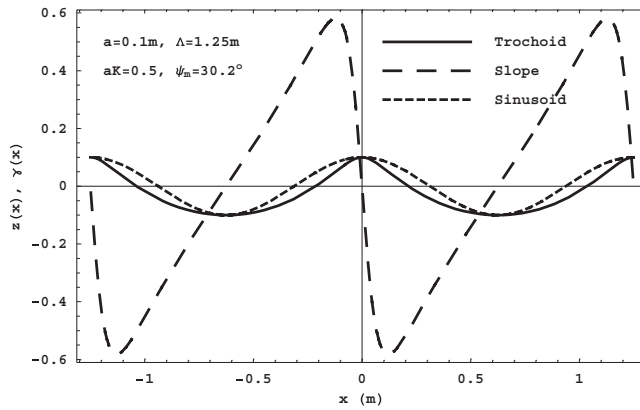


Figure 3. Comparison of the shapes of a sinusoid and a trochoid.

slope shifts closer to the top of the wave (see figure 2). Cycloid is a limiting case of trochoid when $b = 1, \gamma_m = \infty$.

In figure 3 a trochoid and sinusoid with the same amplitude a and wavenumber K are depicted for $aK = 0.5$, which corresponds to the trochoid's maximum slope angle $\psi_m = \arctan \gamma_m = 30.2^\circ$. The figure shows that the trochoid is sharper at the top and flatter at the bottom than the sinusoid, and its maximum slope position is closer to the top than to the bottom. (The maximum slope of the sinusoid is halfway between the top and the bottom.)

3.2. Shadowing

When applying the two-scale model to the wave scattering by a trochoid shape surface, we must take into account the possible partial shadowing of the trochoid's surface for a small grazing angle ψ_0 of the incident wave, when $\gamma_0 \equiv \tan \psi_0 \leq \gamma_m$. The tangent point (the point where the incident ray touches the trochoid) is determined by the equation

$$\gamma = -\frac{b \sin t}{1 - b \cos t} = -\gamma_0. \tag{27}$$

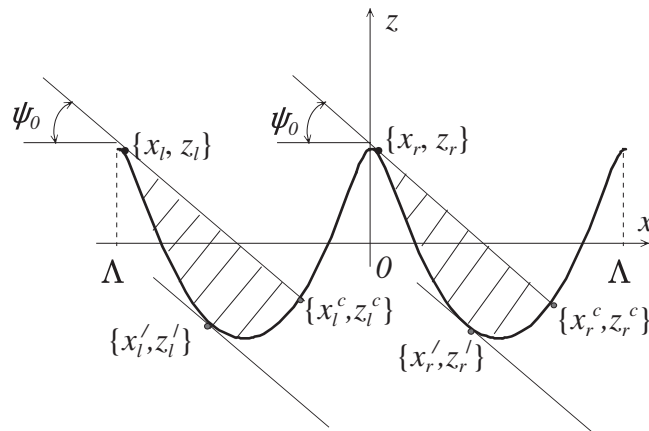


Figure 4. The shadow of trochoid's profile.

It has the following solutions:

$$t_{\pm} = \arccos \frac{\gamma_0^2 \pm \sqrt{b^2(1 + \gamma_0^2) - \gamma_0^2}}{b(1 + \gamma_0^2)}, \quad (28)$$

where only solutions t_+ correspond to the actual tangent points, which separate the illuminated part of the surface from the shadowed part (the upper points $\{x_l, z_l\}$ and $\{x_r, z_r\}$ for two consecutive periods—left $(-\Lambda < x < 0)$ and right $(0 < x < \Lambda)$ —are depicted in figure 4), while the solutions t_- correspond to the points $\{x'_l, z'_l\}$, $\{x'_r, z'_r\}$ and so on, which are located entirely in the shadow (figure 4).

The equation of the light–shadow boundary, for the right-side (r) trochoid's period in figure 4, has the following form:

$$z_s = z_r - \gamma_0(x_s - x_r), \quad (29)$$

where x_r, z_r are the upper touching point coordinates:

$$\begin{aligned} x_r &= t_r/K - a \sin t_r \\ z_r &= a \cos t_r, \end{aligned} \quad (30)$$

and t_r is one of the solutions t_+ , which belongs to the 'right' period $(0 < t < 2\pi)$. The shadowed part of trochoid to the right of point $\{x_r, z_r\}$ (i.e. $x_r < x < \Lambda + x_r$ or $t_r < t < 2\pi + t_r$) is given by the inequality $z_s \geq z(t)$, that is

$$z_r - \gamma_0[t/K - a \sin t - x_r] \geq a \cos t, \quad (31)$$

and, in a geometrical optics approximation, it can be excluded from the integral (13) by multiplying the integrand (14) by a 'shadowing' factor

$$\theta \left[a \cos t - z_r + \gamma_0 \left(\frac{t}{k} - a \sin t - x_r \right) \right], \quad (32)$$

where θ is the Heaviside function

$$\theta(t) = \begin{cases} 1 & \text{for } t > 0 \\ 0 & \text{for } t < 0. \end{cases} \quad (33)$$

The shadowing factor for the 'left' trochoid's period (i.e. $t_l < t < t_r$, or $x_l < x < x_r$) is given by the same expression (32) with the substitutions $(x_r \Rightarrow x_l, z_r \Rightarrow z_l)$, where the coordinates (x_l, z_l) of left-period, upper touching point is given by (30) with the replacement $t_r \Rightarrow t_l = t_r - 2\pi$ that leads to the obvious equations $x_l = x_r - \Lambda$, $z_l = z_r$ (see figure 4).

4. Specific scattering cross sections and Doppler spectra

From (14) and (15), it follows that the specific scattering cross section $\sigma_0(\mathbf{r})$ dependence on sea roughness is determined by a product of two factors: the spatial power spectrum \mathcal{S}_ζ of a small-scale ripples and the scattering coefficient $C(\psi, \mathbf{r})$, which in turn, is proportional to the fourth power of field amplitude $F(\mathbf{r})$ at a smoothed sea surface. Hereafter we ignore the dependence on the first factor and assume for simplicity that \mathcal{S}_ζ is constant over the entire surface. We consider only the spatial distribution (over a large-scale surface) of the scattering coefficient $\tilde{C}(\psi, \mathbf{r}) = C(\psi, \mathbf{r})\sqrt{1 + \gamma^2(\mathbf{r})}$ (normalized by the unit area of plane $z = 0$; see (19)) and its dependence on parameters of the large-scale surface, which is assumed to be a Gerstner's wave, that is, a trochoid.

The scattering coefficient can be considered as a function of only one coordinate x , which we denote as $\sigma(x)$: $\sigma(x) \equiv \tilde{C}(\psi, \mathbf{r})$. Since we have only a parametric equation for the surface shape (23), it is convenient to represent $\sigma(x)$ as a function of the same parameter t :

$$\sigma(t) = \sigma(x) \left| \frac{dx}{dt} \right| = \sigma[x(t)] \left| \frac{1}{k} - a \cos t \right|, \quad (34)$$

where $x(t) = t/K - a \sin t$, according to (23). The set of these two equations for $\sigma(t)$ and $x(t)$ can be considered as a parametric representation of the function $\sigma(x)$, that is, the spatial distribution of a specific backscattering cross section ('radar brightness') over the longitudinal coordinate x .

Equations (14) and (15) enable us to obtain the backscattered power from every point of a given large-scale surface. Since the distribution of orbital velocity vectors \mathbf{v} over the surface is known, it is possible to link the specific frequency shift to a particular point of the surface with known backscattering cross section $\sigma(x)$, and to calculate the total Doppler spectrum S_D of backscattered wave. For an incident plane wave the Doppler frequency shift is equal to $\Delta\omega = 2\mathbf{k}\mathbf{v}$, where the wavevector \mathbf{k} was introduced in (8) and components of orbital velocity \mathbf{v} are given by (24). This frequency shift $\Delta\omega$ is a function of surface coordinates, but since we have only a parametric equation for the surface shape (23), it is convenient to represent $\Delta\omega$ as a function of parameter t , too:

$$\Delta\omega = \omega_m \cos(\psi_0 + t), \quad (35)$$

where $\omega_m = 2kv_0$. Hereafter we consider the reduced frequency shift f normalized by the maximum value ω_m : $f(t) = \Delta\omega/\omega_m = \cos(\psi_0 + t)$.

The parametric representation of the Doppler spectrum $S_D(f)$ follows from the obvious relation

$$S_D(f) = \sum_{j=1}^2 \sigma(t_j) \left| \frac{df(t)}{dt} \right|_{t_j}^{-1}, \quad (36)$$

where $t_j = t_j(f)$ are the solutions of the equation $f = \cos(\psi_0 + t)$. Notice that in one trochoid's period there are two points, t_1 and t_2 , with the same projection of orbital velocity vector \mathbf{v} on the wavevector \mathbf{k} (i.e. with the same Doppler shift f), which are related as follows: $t_2 = 2(\pi - \psi_0) - t_1$. Only for maximum frequency shifts $f = \pm 1$, these two points merge into one: $t = \psi_0$ (for $f = 1$) and $t = \pi - \psi_0$ (for $f = -1$). Thus, for parametric representation of S_D we obtain

$$S_D(t) = \frac{\sigma(t) + \sigma(2\pi - 2\psi_0 - t)}{|\sin(\psi_0 + t)|}, \quad (37)$$

$$f(t) = \cos(\psi_0 + t)$$

where parameter t corresponds to the half-period of the trochoid ($-\psi_0 < t < \pi - \psi_0$).

To obtain the functions $\sigma(x)$ and $S_D(f)$ in explicit form, we must define the only remaining unknown function $F(\mathbf{r})$, the spatial distribution of incident wave amplitude over the trochoid's surface.

4.1. Geometrical optics approach

In the geometrical optics (or tangent plane) approximation, function $F(\mathbf{r})$ is given by (16), and together with (15), (19), and (34), we obtain the following backscattering cross section dependence on parameter t (omitting factor $16\pi k^4 S_\zeta(2k \cos \psi, 0)$ from (14)):

$$\sigma(t) = |1 - \eta^2 + \cos^2 \psi|^2 \left| \frac{\sin \psi}{\sin \psi + \eta} \right|^4 \sqrt{1 + \gamma^2} \left| \frac{1}{k} - a \cos t \right|, \quad (38)$$

where $\psi = \psi_0 + \arctan \gamma$ is a local grazing angle, and $\gamma = \gamma(t)$ is given by (25). This equation is valid only if $\tan \psi_0 > \gamma_m$, when there is no shadowing. When $\tan \psi_0 < \gamma_m$, it is necessary to take into account that in shadow zones $F = 0$ and consequently $\sigma = 0$. This can be achieved by multiplying (38) by the 'shadowing' factor (32) for the interval $t_r < t < 2\pi + t_r$ (i.e. for $x_r < x < \Lambda + x_r$; see figure 4). For the interval $t_l < t < t_r$, the following substitutions must be made in expression (32): $t_r \Rightarrow t_l = t_r - 2\pi$; $x_r \Rightarrow x_l = x_r - \Lambda$ (see figure 4).

The backscattering specific cross sections $\sigma_{h,v}(x)$ and Doppler frequency power spectra $S_{h,v}(f)$, which are functions $S_D(f)$ normalized on the total backscattered power $\int_{-1}^1 S_D(f) df$, are plotted in figure 5 for two polarizations, which are indicated by subscripts: h (horizontal) and v (vertical). The curves were plotted for the trochoid with the following parameters (see figure 3): $a = 0.1$ m, $\Lambda = 1.25$ m, $b = 0.5$ and grazing angles $\psi_0 = 5^\circ, 10^\circ, 28^\circ$ and 40° . The complex dielectric permittivity of sea water was chosen as $\varepsilon = 60 + 30i$ (the mean value for SHF radio wave X-band). Because of the geometrical optics approximation, the spatial distribution of the backscattering cross sections $\sigma_{h,v}(x)$ and normalized frequency power spectra $S_{h,v}(f)$ do not depend on the linear scales a and Λ separately, but remain the same for all trochoids with fixed steepness parameter $b = 2\pi a/\Lambda$ and arbitrary amplitudes and periods. We chose 0.5 for the value of parameter b , because it corresponds to the maximum slope $\gamma_m = 0.58$, or $\psi_m = 30.2^\circ$, which is close to the limiting slope ($\simeq 30^\circ$) of Stokes's wave. The thin solid curves in the upper panels in figures 5(a), (b) correspond to the trochoid's profile with parameters $a = 0.1$ m and $\Lambda = 1.25$ m (linear scales there are in meters) and $\theta(x)$ is the shadowing function depicted as a thin dashed line.

For all grazing angles, $\sigma_v(x)$ exceeds $\sigma_h(x)$, and their difference increases with decreasing the grazing angle ψ_0 . The spatial variation of these curves (thick solid curves for v —polarization, and thick dashed ones for h —polarization) is caused by the variation of the local grazing angle ψ along the surface (see figure 1). For a steep grazing angle ψ_0 of 40° , there is no shadowing of the surface: $\theta(x) = 1$ for all x . The maximum of $\sigma_h(x)$ and one of the minima of $\sigma_v(x)$ correspond to the point of the surface profile $z(x)$ where the local grazing angle ψ is maximal. This point is closer to the trochoid's crest than to its trough (in contrast with the sinusoid, for which this point is always halfway between the crest and the trough). The second minimum of $\sigma_v(x)$ corresponds to the point of the trochoid's where the local grazing angle ψ is a minimum, if it is less than the Brewster angle $\psi_B \simeq \arcsin(1/\sqrt{\varepsilon})$.

At $\psi_0 = 28^\circ$, only slightly less than the trochoid's maximum slope ψ_m of 30.2° , the surface shadows appear at $0.07 \lesssim x \lesssim 0.27$ m for the right-hand trochoid's period and at $-1.18 \lesssim x \lesssim -0.98$ for the left-hand one. The linear size of shadowed surface part increases with decreasing grazing angle ψ_0 , and for $\psi_0 = 5^\circ$, the illuminated part of surface where $\theta(x) = 1$, it is equal to only $\simeq 0.2$ m (see the right upper panel in figure 5(b)).

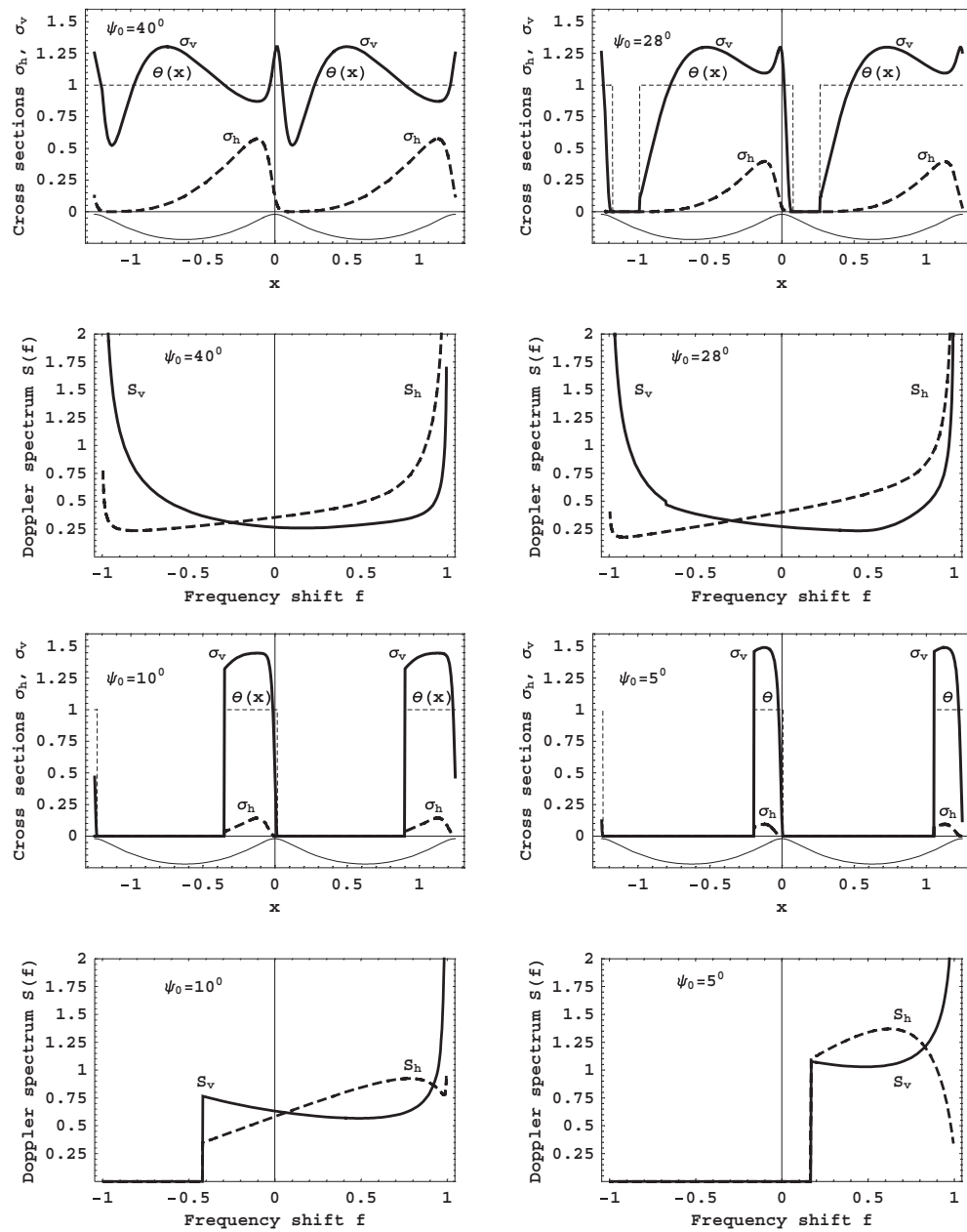


Figure 5. Geometrical optics results for the spatial distribution of specific backscattering cross sections (upper panels) and Doppler frequency spectra (lower panels) for two grazing angles: (a) $\psi_0 = 40^\circ$ and 28° , and (b) $\psi_0 = 10^\circ$ and 5° . Vertical polarization—solid thick curves; horizontal polarization—dashed thick curves; the trochoid's profile ($a = 0.1$ m, $\Lambda = 1.25$ m, $aK = 0.5$)—thin solid curve and the thin dashed curve is the shadowing function.

The shadowing eliminates the negative frequencies in the Doppler spectra, which originate from the radio waves scattered by the troughs, and for the extreme grazing angle ψ_0 of 5° , when only trochoid's crests are illuminated (see the right panel in figure 5(b)) the spectra

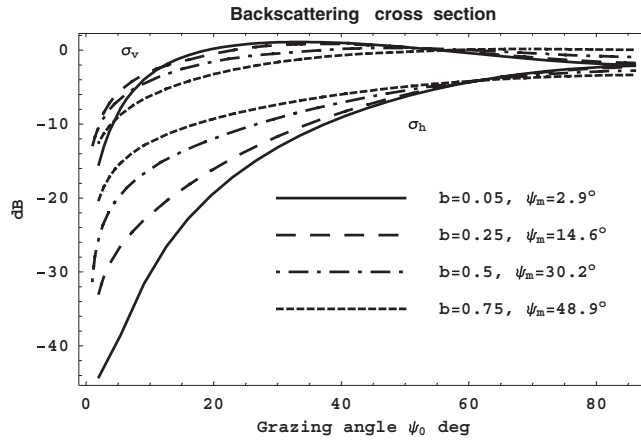


Figure 6. Spatially averaged specific backscattering cross sections for trochoids with different steepness parameters b and maximum slopes ψ_m . The upper set of curves corresponds to vertical polarization; the lower, to horizontal polarization.

become much narrower than those for the completely illuminated surface. It is worthwhile pointing out that the Doppler spectra for h - and v -polarized waves have the opposite skewness: toward positive frequencies for the h -polarized radar signal, and toward negative frequencies for the v -polarized one.

In figure 6 the mean specific backscattering cross sections $\bar{\sigma}$, averaged over the space coordinate x :

$$\bar{\sigma} = \frac{1}{\Lambda} \int_0^{\Lambda} \sigma(x) dx, \quad (39)$$

are represented for a set of trochoids with different steepness parameters b or corresponding angles of maximum slopes ψ_m . The upper set of curves corresponds to the vertical polarization $\bar{\sigma}_v$, and the lower one corresponds to the horizontal polarization $\bar{\sigma}_h$. Remember that $\sigma(x)$ and $\bar{\sigma}$ represent only the diffuse part of backscattered signal due to the scattering by small ripples. For steep grazing angles $\psi_0 \gtrsim \psi_m$, specular reflections in backward direction appear, which give the dominant contribution to the total backscattered power; however, their contribution is not represented in figure 6.

From figure 6 it follows that $\bar{\sigma}_h$ is more sensitive to the Gerstner's wave steepness b than $\bar{\sigma}_v$, and this difference becomes smaller as the surface wave becomes steeper.

The dependence of the mean Doppler frequency shift,

$$\bar{f} = \int_{-1}^1 f S(f) df, \quad (40)$$

on grazing angle ψ_0 is depicted in figure 7 for the same set of surface steepness parameters b as in figure 6. The upper curves in this plot correspond to horizontal polarization and the lower to vertical polarization. Excluding the extreme grazing angles, the mean Doppler frequency shift for horizontal polarization is positive. (The radar supposedly illuminates the surface in the 'upwind' direction, i.e. opposite that of the surface wave propagation.) The mean Doppler frequency shift for horizontal polarization exceeds that for vertical polarization, which is mostly negative for non-grazing incidence ($\psi_0 \gtrsim 20^\circ$). This difference increases with increasing steepness of the surface wave. The explanation is that the local grazing angles ψ for rear faces and troughs of the surface wave, which scatter radio waves with a negative Doppler frequency,

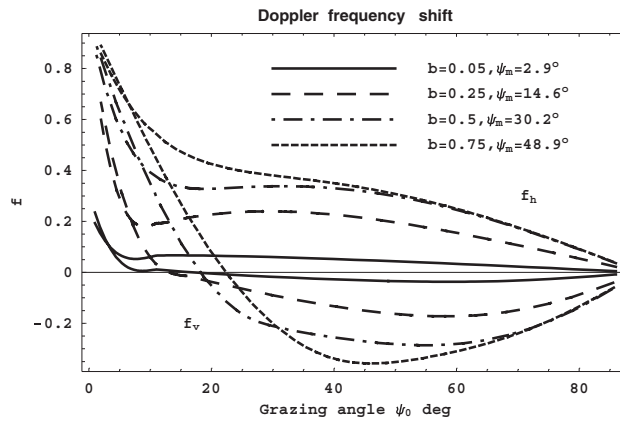


Figure 7. Mean Doppler frequency shifts (normalized on the maximum value) for trochoids with different steepness parameters b and maximum slopes ψ_m . The upper curves correspond to horizontal polarization; the lower, to the vertical polarization.

are smaller than the grazing angles for front faces, which cause a positive Doppler shift. Since the specific backscattering cross section for horizontal polarization decreases rapidly as $\sim \psi^4$ at low grazing angles, these negative Doppler frequencies are significantly suppressed, which leads to the positive mean value of the Doppler frequency. For small grazing angles $\psi_0 < \psi_m$, the Doppler frequency shifts for two polarizations are almost the same, because, in this case, only surface wave crests are illuminated, and their movement causes the same Doppler frequency shift for both polarizations.

4.2. Diffraction by a trochoid

Taking into account the multiple scattering and diffraction of a zero-order field U_0 by the smooth trochoid (without Bragg-resonant scattering ripples) leads to a change in the wave amplitude $F(\mathbf{r})$ from its geometrical optics value. The scattering coefficient $C(\psi, \mathbf{r})$ (see (15)) and the specific scattering cross section $\sigma_0(\mathbf{r})$ given by (14) are modified correspondingly. Since we are assuming that the wave amplitude $F(\mathbf{r})$ still varies much slower than the phase factor e^{ikr} , and that the Doppler frequency shift $\Delta\omega$ from every surface element is equal to $2k\mathbf{v}$, as before, we neglect the very fast oscillation of the field amplitude $F(\mathbf{r})$, as well as the deviation of the wave propagation direction right near the surface from the direction of wavevector \mathbf{k} for an incident wave (and $-\mathbf{k}$ for a backscattered wave). It is worth emphasizing that in what follows we consider the backscattering from the same rough surface (smooth trochoid covered by small-scale random ripples), but now the zero-order field amplitude $F(\mathbf{r})$ is obtained not in geometrical optics approximation, but using a rigorous numerical solution of the diffraction problem, which takes into account multiple scattering as well as diffraction effects caused by a trochoid. Scattering by small-scale ripples is calculated by the first order of small perturbation theory as before.

The numerical method for solving the appropriate diffraction problem is described in detail in [14]. The outline of the approximate version of the method is also given in [13]. The diffraction code used is based on the numerical solution of the integral equation for the total surface field in a two-dimensional case. It uses an impedance boundary condition. The numerical solution is facilitated by representation of the field at the surface as a product of the fast-oscillating phase factor corresponding to the incident wave, and another factor, which appears to be slow varying on a wavelength-scale.

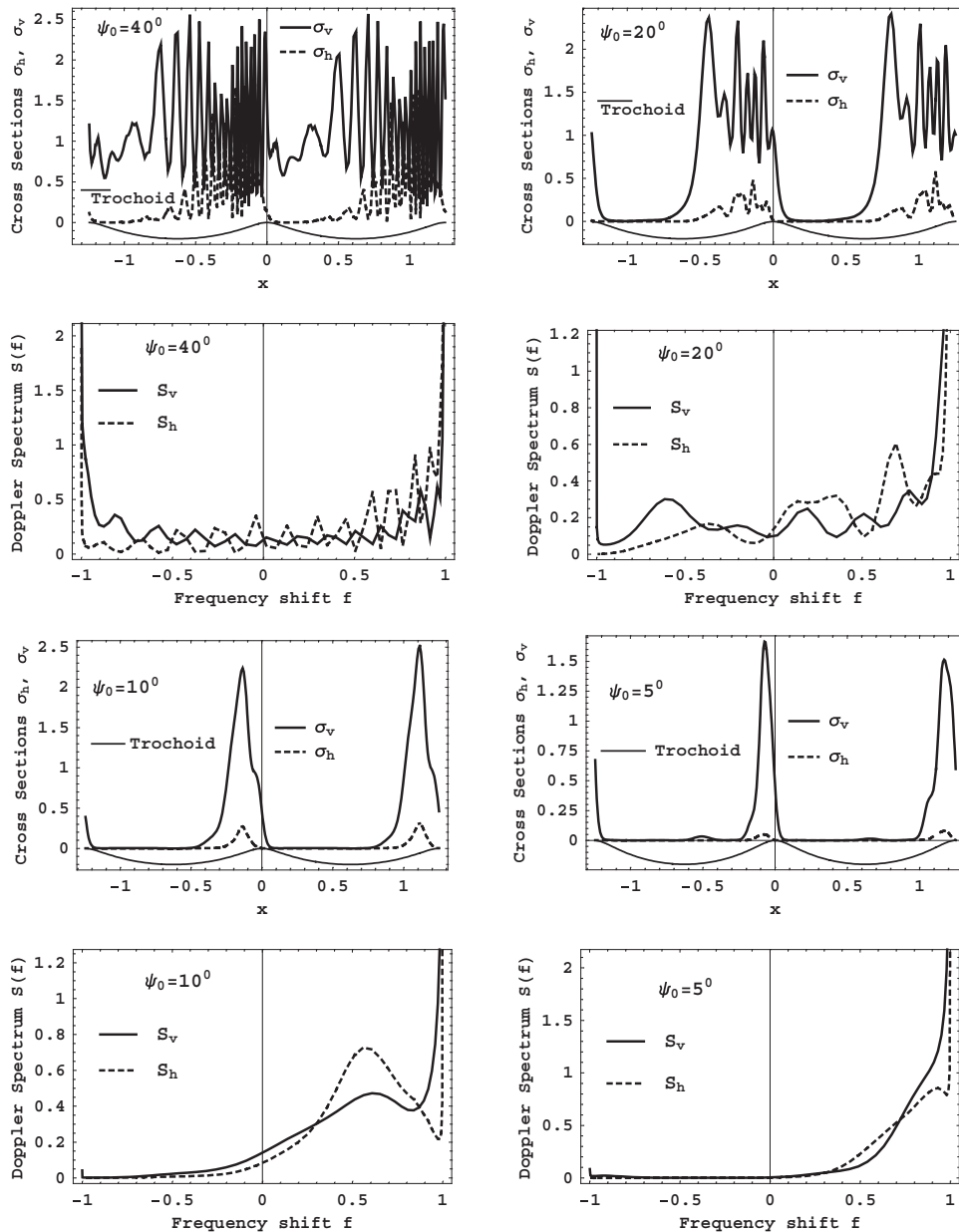


Figure 8. ‘Exact’ diffraction results for spatial distribution of specific backscattering cross sections (upper panels) and Doppler frequency spectra (lower panels) for four grazing angles: (a) $\psi_0 = 40^\circ$ and 20° , and (b) $\psi_0 = 10^\circ$ and 5° . Vertical polarization—solid thick curves; horizontal polarization—dashed thick curves; the trochoid’s profile ($a = 0.1$ m, $\Lambda = 1.25$ m, $aK = 0.5$)—thin solid curve.

Figures 8(a), (b) depicts a set of plots for backscattering specific cross sections $\sigma_{h,v}(x)$ and the Doppler frequency power spectra $S_{h,v}(f)$ for the same set of trochoid parameters as in figures 5(a), (b) ($a = 0.1$ m, $\Lambda = 1.25$ m, $b = 0.5$, $\psi_m = 30.2^\circ$, $\varepsilon = 60 + 30i$), grazing angles: ψ_0 of 5° , 10° , 20° , 40° , and an incident radio wavelength $\lambda = 0.02$ m. The thin solid

curves in the upper panels in figures 8(a), (b) correspond to the trochoid's profile (linear scales are in meters). The very strong oscillations of the specific backscattering cross sections $\sigma_{h,v}(x)$ appear at a steep grazing angle, $\psi_0 = 40^\circ$, owing to the interference of multiple scattered fields at the trochoid's surface. The validity of such an interpretation follows from the fact that for very steep incident angles, $\psi_0 > 60^\circ$, when the probability of multiple scattering tends to zero, since $\psi_m < 30^\circ$, these oscillations disappear. We do not show these plots because they are very similar to the plots of the geometrical optics results.

At a lower grazing angle, $\psi_0 = 20^\circ$, the period of these oscillations increases because the propagation of interfering waves along the surface becomes more grazing than for the case of $\psi_0 = 40^\circ$, supporting the concept that these oscillations are caused by the interference of multiple scattered waves.

The geometrical shadow with very small cross section values $\sigma_{h,v}(x)$ is clearly seen in plots for $\psi_0 = 5^\circ, 10^\circ, 20^\circ$. For a moderate grazing angle, $\psi_0 = 20^\circ$, the field oscillations just above the shadow boundary are caused partially by the wave diffraction by the trochoid's edge (not only by the interference of multiple scattered waves). Unlike the geometrical optics results represented in the upper panels of figure 5(b), the boundary between the shadowed and illuminated (by the incident wave) parts of the surface is not too sharp, and, for the extreme grazing angles ($\psi_0 = 5^\circ, 10^\circ$) there are no field oscillations in the illuminated area. This fact agrees with the conclusions made in [18] that the effect of multiple reflections on a scattered field becomes negligible at very small grazing angles. The oscillations due to the wave diffraction by the trochoid's crest are also absent at $\psi_0 = 5^\circ, 10^\circ$, because the vertical size of illuminated part of the surface ($\sim \Lambda \tan \psi_0$) is less than that of the first Fresnel zone ($\sim \sqrt{\lambda/\Lambda}$) at a distance from the crest equal to the trochoid's period Λ .

The spatial oscillations of the specific backscattering cross sections shown in the upper panels in figure 8(a), cause the corresponding oscillations of the Doppler frequency spectra shown in the lower panels in figure 8(a). The opposite sign of the averaged Doppler spectra skewness can be seen, but not so clear as in geometrical optics results (lower panels in figure 5(a)). For horizontal polarization the positive Doppler frequencies predominate, and for vertical polarization the negative ones. For small grazing angles $\psi_0 = 5^\circ, 10^\circ$, the Doppler frequency spectra (lower panels in figure 8(b)) become narrower and shift to the positive Doppler frequencies for both polarizations. In this case, only a very small part of the surface in the vicinity of the trochoid's crests (with an almost constant orbital velocity) takes part in the scattering.

Despite the very different appearance of the geometrical optics and diffraction results for scattering cross sections and Doppler frequency spectra represented in figures 5(a), (b) and figures 8(a), (b), the mean values of the specific scattering cross sections $\bar{\sigma}$ and the mean Doppler frequency shift \bar{f} , introduced by (39) and (40) correspondingly, are unexpectedly close. In figure 9 the solid curves correspond to the $\bar{\sigma}$ obtained in the geometrical optics approach, and results of the diffraction approach are presented by data points. For very steep grazing angles, results of the two approaches agree very well. For moderate grazing angles, the specific scattering cross sections $\bar{\sigma}$ obtained by taking into account the diffraction and multiple scattering effects exceed the geometrical optics ones. This difference is greater for the horizontal polarization because the Fresnel reflection coefficient for horizontal polarization is always larger than that for vertical polarization. Therefore the multiple scattering plays a more essential role for horizontal polarization, giving the remarkable rise to the total scattering cross section. This fact agrees with the result of qualitative consideration of role of double scattering processes in backscatter from sea surface [19, 20], as well as with the analytical and numerical results for radio wave multiple scattering from concave rough surface [12].

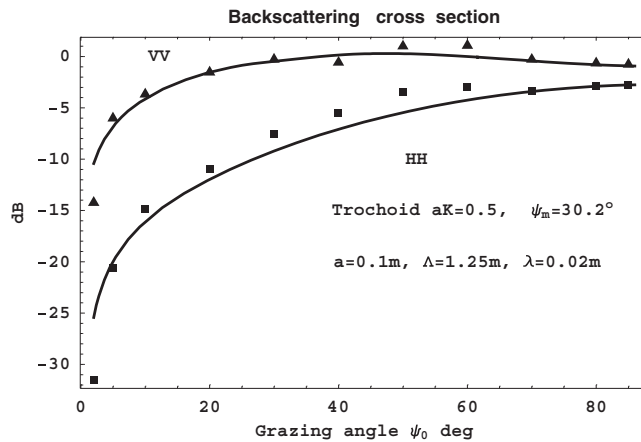


Figure 9. Comparison of geometric optics results for averaged specific backscattering cross sections (solid curves) with their 'exact' values (multiple scattering and diffraction effects have been taking into account): triangles for vertical polarization and squares for horizontal polarization.

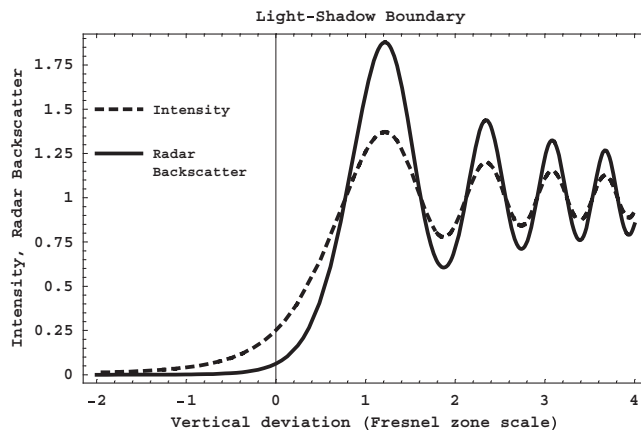


Figure 10. The intensity (dashed curve) and radar backscatter (solid curve) spatial distribution near the geometric optics light-shadow boundary.

At low grazing angles when the multiple scattering processes do not play an essential role, these two approaches give similar results again. At last, at extremely low grazing angles (in figure 9 the minimal grazing angle ψ_0 is equal to 2°), the geometrical optics result for $\bar{\sigma}$ exceeds significantly the value given by the diffraction approach. This difference can be explained by considering the wave field intensity distribution (figure 10) in the vicinity of the light-shadow boundary in the left-hand face of the trochoid's crest (the incident wave propagates from the left to the right as it shown in figure 1). The geometrical optics boundary position is located at zero elevation; the negative elevations correspond to shadow (where the zero-order field amplitude $F(r)$ is zero) and the positive elevations are illuminated by the incident wave with an amplitude $F(r) = 1$. Diffraction of the incident wave by the next trochoid's crest to the left (which we may consider here as a vertical half-plane for simplicity) results in the broadening of the light-shadow boundary, and, which is more important, is its shift from zero to the higher heights (positive values of 'vertical displacement' along the abscissa axis in figure 10) for a distance

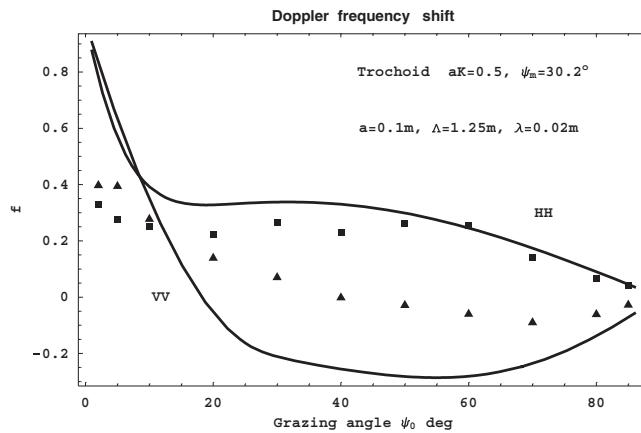


Figure 11. Comparison of geometric optics results for mean Doppler frequency shifts (solid curves) with their 'exact' values (marks), taking into account multiple scattering and diffraction effects.

that is equal to about one Fresnel zone ($\sim\sqrt{\lambda\Lambda} \simeq 16$ cm). Meanwhile, the total vertical size of the illuminated part of the trochoid's left-hand face is equal only to $\sim\Lambda\psi_0 \simeq 4$ cm for $\psi_0 = 2^\circ$. From these very rough estimates, it follows that in the illuminated part of the surface (above the geometrical optics shadow boundary and below the trochoid's crest) the intensity $F^2(\mathbf{r})$ of the incident wave (dashed curve in figure 10) is significantly less than unity, and therefore the backscattering cross section, which is proportional to $F^4(\mathbf{r})$ (see (14), (15)) can be several times less than the geometrical optics value. In figure 9 this difference between geometrical optics and diffraction results at $\psi_0 = 2^\circ$ is equal to $\simeq 4$ dB for vertical polarization and $\simeq 6$ dB for horizontal polarization.

In figure 11 the mean Doppler frequency shift \bar{f} , introduced in (39), is depicted with the same notations used in figure 9. The diffraction and multiple scattering processes result in less the difference in \bar{f} between vertical and horizontal polarization (triangles and squares in figure 11) than that obtained with the geometrical optics approach (solid lines in figure 11). Only for the very steep grazing angles, do the results of the two approaches coincide. For the very low grazing angles, $\psi_0 \leq 10^\circ$, the difference between the mean Doppler frequency shifts \bar{f} for vertical and horizontal polarization is very small, but for the diffraction approach both of these shifts are about half as large as the shifts the geometrical optics approach. This effect is the result of the illuminated area spreading due to the incident wave diffraction by the next left trochoid's crest. In addition to backscattering from a very small part of the trochoid's face (above the geometrical optics shadow boundary and below the trochoid's crest, which has an almost constant orbital velocity) there is backscattering from a much larger surface area, with a wider range of orbital velocities. The result is the broadening of the Doppler frequency spectra $S(f)$ and a decrease in the mean frequency shift \bar{f} for both polarizations.

5. Conclusions

We employed the two-scale model for solving a problem of SHF-EHF radio wave scattering by a large-scale (in comparison with radio wavelength) nonlinear Gerstner's water-surface wave (i.e. trochoid) covered by resonant-Bragg-scattering small ripples. The expressions for backscattering cross sections and Doppler spectra can be expressed in terms of a zero-order field that incorporates diffraction effects due to the long-wave component of the surface.

Two approaches were used for finding the zero-order field: the geometrical optics (tangent-plane or Kirchhoff approximation) method and an 'exact' (numerical) solution of diffraction by trochoid. We assumed that the density of Bragg scatterers does not vary along the Gerstner's wave profile, and that the effects of phase velocity of ripples could be neglected.

We determined that even in geometrical optics approach, the modulation of Bragg backscattering cross sections by trochoid's slopes leads to the essentially nonuniform spatial distribution of specific backscattering cross sections along the trochoid's surface. Horizontal polarization is more sensitive to this slope-caused modulation than vertical polarization, especially at low grazing angles. The difference between space-averaged backscattering cross sections with horizontal and vertical polarizations (HH/VV ratio) at low grazing angles decreases rapidly with surface slope increases: from $\simeq 30$ dB for a gentle trochoid with a maximum slope $\psi_m \simeq 3^\circ$ to $\simeq 7$ dB for a steep trochoid with maximum slope $\psi_m \simeq 50^\circ$.

The difference between spatial distribution along the trochoid's profile of the cross sections for vertical and horizontal polarizations leads to skewness of the Doppler frequency spectra with opposite signs: for horizontal polarization the positive Doppler frequency shifts predominate (for waves moving towards the radar) and for vertical polarization, the shift is negative. At very low grazing angles, the Doppler frequency spectra become narrower, concentrating near the maximum positive frequency, and difference of the mean Doppler frequency shifts between two polarizations vanishes. However, at moderate grazing angles and steep waves, it can attain $\simeq 80\%$ of the maximum Doppler frequency, which corresponds to the maximal orbital velocity of liquid particles in Gerstner's wave.

The 'exact' solution of the radio-wave diffraction problem for zero-order field (smooth trochoid without ripples) produces the results that are significantly different from those of the geometrical optics approach. Very strong oscillations appear in the specific cross-section spatial distribution as well as in the Doppler frequency spectra. These oscillations are caused by interference of multiple scattered waves and diffraction by the trochoid's crests. These oscillations disappear only at very low and very steep grazing angles, and the diffraction by the trochoid's crests results in smaller backscattering cross sections than the geometrical optics results. This effect can be interpreted by the specific pattern of the field (shifting up the effective shadow-light boundary relative to its geometrical optics position) diffracted by the half-plane screen, which models the trochoid's crest. Despite tremendous differences in the details of the results obtained by the geometrical optics and diffraction approaches, the mean values of the backscattered-field parameters considered (mean backscattering cross section $\bar{\sigma}$ as well as mean Doppler frequency shift \bar{f}) do not differ so dramatically, and remaining the differences can be explained by a simple, semi-qualitative consideration.

References

- [1] Bass F G, Fuks I M, Kalmykov A I, Ostrovski I E and Rosenberg A D 1968 Very high frequency radio wave scattering by a disturbed sea surface, Pt I and Pt II *IEEE Trans. Antennas Propag.* **16** 554–68
- [2] Barrick D E 1972 First-order theory and analysis of MF/HF/VHF scatter from the sea *IEEE Trans. Antennas Propag.* **20** 2–10
- [3] Weber B L and Barrick D E 1977 On the nonlinear theory for gravity waves on the ocean surface. Pt I: derivations *J. Phys. Oceanogr.* **7** 3–10
- [4] Barrick D E and Weber B L 1977 On the nonlinear theory for gravity waves on the ocean surface. Pt II: interpretation and applications *J. Phys. Oceanogr.* **7** 11–21
- [5] Kur'yanov B F 1962 The scattering of sound at a rough surface with two types of irregularity *Sov. Phys.-Acoust.* **8** 252–7
- [6] Fuks I M 1966 To the theory of radio wave scattering by a disturbed sea surface *Radiophys. Quantum Electron.* **9** 513–9
- [7] Valenzuela G R and Laing M B 1970 Study of Doppler spectra of radar sea echo *J. Geophys. Res.* **75** 551–63

- [8] Bass F G and Fuks I M 1972 *Wave Scattering from Statistically Rough Surfaces* (Moscow: Nauka) (in Russian) (Engl. transl. 1978 *Int. Series in Natural Philosophy* vol 93, ed C B Vesecky and J F Vesecky (Oxford: Pergamon))
- [9] Valenzuela G R 1978 Theories for the interaction of electromagnetic and oceanic waves—a review *Bound.-Layer Meteorol.* **31** 61–5
- [10] Fuks I M, Tatarskii V I and Barrick D E 1999 Behaviour of scattering from a rough surface at small grazing angles *Waves Random Media* **9** 295–305
- [11] Fuks I M and Voronovich A G 1998 Multiple radio wave scattering by sea surface at low grazing angles *Proc. IEEE Int. Geoscience Remote Sensing Symp. (July 1998, Seattle, WA, USA)* vol 4 (Piscataway, NJ: IEEE) pp 2284–8
- [12] Fuks I M and Voronovich A G 1999 Wave diffraction by a concave statistically rough surface *Waves Random Media* **9** 501–20
- [13] Voronovich A G and Zavorotny V U 2000 The effect of steep sea-waves on polarization ratio at low grazing angles *IEEE Trans. Geosci. Remote Sens.* **38** 366–73
- [14] Voronovich A G and Zavorotny V U 2000 Simulation of microwave backscattering from rough surfaces at low grazing angles: An effective numerical algorithm *NATO RTO Meeting Proc. 60: Low Grazing Angle Clutter: Its Characterization, Measurement and Application (April 2000, MD, USA)* (Hull, Canada: St. Joseph Corporation Company) pp 12(1–9)
- [15] Toporkov J V 2000 Numerical simulations of scattering from time-varying, randomly rough surfaces *IEEE Trans. Geosci. Remote Sens.* **38** 1616–25
- [16] Lamb H 1995 *Hydrodynamics* 6th edn (New York: Cambridge University Press)
- [17] Kamenkovich V M and Monin A C 1978 *Ocean Physics* vol 2 (Moscow: Nauka)
- [18] Mikhailova D V and Fuks I M 1993 Emissivity of a statistically rough surface including multiple reflections *J. Commun. Technol. Electron.* **38** 128–36
- [19] Hanson S G and Zavorotny V U 1995 Polarization dependency of enhanced multipath radar backscattering from an ocean-like surface *Waves Random Media* **5** 159–65
- [20] Trizna D B 1997 A model for Brewster angle damping and multipath effects on the microwave radar sea echo at low grazing angles *IEEE Trans. Geosci. Remote Sens.* **35** 1232–44